Algorithm Theoretical Basis Document Rongowai GNSS-R Level 1B Calibration

Prepared by Xiaoyou Lin

March 5, 2024

(L1 Calibration Algorithm Version: 2.4)

1 Level 1b Calibration Approach

This document is the second part of the overall Level 1 Calibration Algorithm Theoretical Basis Document (ATBD) describing the Level 1b calibration for Rongowai. The algorithms described here have significant heritage from the CYGNSS mission [1], [2] but is customised for the airborne geometry and flight characteristics of Rongowai on the Air New Zealand domestic aircraft and the new capabilities of the Next-generation receiver (NgRx) [3].

The Level 1b calibration is performed after the Level 1a calibration and uses external meta-data to convert the Level 1a power in watts to a delay-Doppler map (DDM) map of normalised bistatic radar cross section (NBRCS) values. This conversion is done for every pixel in every DDM and uses the following information collected coincident with the science DDM:

1) The aircraft GPS time, position and velocity in the WGS84 Earth-Centered Earth-fixed (ECEF) reference frame.

2) The GNSS satellite position and velocity in the WGS84 ECEF reference frame.

3) Detailed knowledge of the aircraft nadir antenna patterns.

4) Attitude knowledge of the aircraft at the time of the measurement.

5) An estimate of the GPS effective isotropic radiative power (EIRP) in the direction of the specular reflection point in the GNSS satellite reference frame.

Additional information calculated using the per DDM science meta-data and used in the Level 1b calibration of each DDM includes:

1) An accurate surface geolocation of the reflection specular point (SP) in the WGS84 ECEF reference frame.

2) A precise estimate of the specular reflection point location in the measurement DDM pixel delay and Doppler bins.

3) The path length between the GNSS satellite and specular reflection point and between the specular reflection point and the aircraft.

4) The effective scattering area per DDM bin surrounding the specular point over all delay and Doppler bins.

The above parameters are then used to estimate values of the bistatic radar cross section (BRCS) and reflectivity for each DDM pixel using the forward model described below.

The flowchart of Rongowai Level 1 calibration is illustrated in Figure 1.

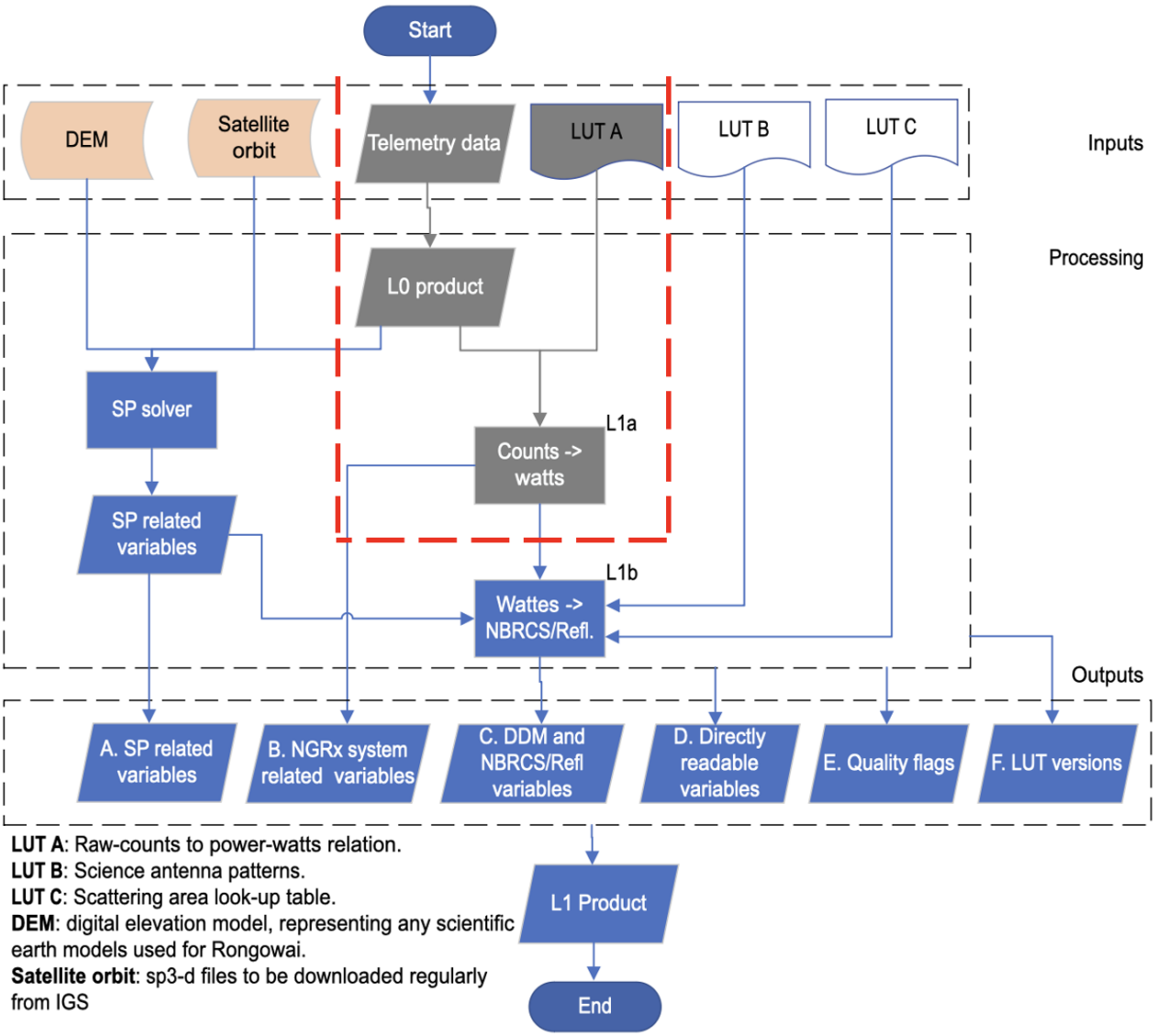

Figure 1: Flowchart of Rongowai Level 1 Calibration and Products.

2 Forward Model of Scattered Signal Power

2.1 Incoherent Reflection

A full expression for the GPS scattered signal power has been previously derived and published in 2000 [4]:

$$P^{g}_{\hat{\tau},\hat{f}} = \frac{P^{T}\lambda^{2}}{(4\pi)^{3}} \iint_{A} \frac{G^{T}_{x,y} G^{R}_{x,y} \sigma^{0}_{x,y}}{(R^{T}_{x,y} R^{R}_{x,y})^{2}} \Lambda^{2}_{\hat{\tau};x,y} S^{2}_{\hat{f};x,y} \mathrm{d}x\mathrm{d}y, \tag{1}$$

where $P^{g}_{\hat{\tau},\hat{f}}$ is the coherently processed scattered signal power, P^{T} is the GNSS satellite transmit power, G^{T} is the GNSS satellite antenna gain. G^{R} is the receiver antenna gain, R^{T} and R^{R} are the transmitter to surface and surface to receiver ranges, respectively, λ is the GNSS signal carrier wavelength (approx. 19 cm for GPS L1 frequency band). $\Lambda_{\hat{\tau}}$ is the GNSS

signal spreading function in delay and $S_{\hat{f}}$ is the frequency response of the GNSS signal. A is the surface integration area covering the effective region of diffuse scattering for each delay Doppler bin and σ^0 is the normalised bistatic scattering cross section (NBRCS).

In the case of Rongowai, the scattered signal power is coherently integrated over a selectable interval (up to 10 ms) for the range of sampled relative delays $\hat{\tau}$ and Doppler frequencies $\hat{f}$, followed by further non-coherent averaging to a 1 second record. The delay and frequency bins map non-uniquely to the scattering surface.

The above expression can be simplified using the effective values of several variables across delay and Doppler bins under the integrand of Eq. 1. The effective values include the effects of delay and Doppler spreading functions, Λ and S, which have been eliminated from the Equation and are indicated by the over-bar in the following equations.

$$P^g_{\hat{\tau},\hat{f}} = \frac{\lambda^2}{(4\pi)^3} \frac{P^T \overline{G}^T_{\hat{\tau},\hat{f}} \overline{G}^R_{\hat{\tau},\hat{f}}}{(\overline{R}^T_{\hat{\tau},\hat{f}} \overline{R}^R_{\hat{\tau},\hat{f}})^2} < \sigma^0_{\hat{\tau},\hat{f}} > \overline{A}_{\hat{\tau},\hat{f}}, \tag{2}$$

where $\overline{G}^R_{\hat{\tau},\hat{f}}$ is the effective receiver antenna gain at each delay-Doppler bin, $\overline{R}^T_{\hat{\tau},\hat{f}}$ and $\overline{R}^R_{\hat{\tau},\hat{f}}$ are the effective ranges at each delay-Doppler bin, and $\overline{A}_{\hat{\tau},\hat{f}}$ is the effective scattering area at each delay-Doppler bin.

2.2 Coherent Reflection

For coherent reflection the area of collection is approximately equal to the first Fresnel zone (FFZ), much smaller than the area of collection corresponding to diffuse scattering. The coherent component can be expressed by the Friis transmission equation form of Eq. 1:

$$P^g_{\hat{\tau},\hat{f}} = \left(\frac{\lambda}{4\pi}\right)^2 \frac{P^T \overline{G}^T_{\hat{\tau},\hat{f}} \overline{G}^R_{\hat{\tau},\hat{f}}}{(\overline{R}^T_{\hat{\tau},\hat{f}} + \overline{R}^R_{\hat{\tau},\hat{f}})^2} \Gamma_{\hat{\tau},\hat{f}}, \tag{3}$$

where $\Gamma_{\hat{\tau},\hat{f}}$ is the reflectivity at each delay-Doppler bin.

3 Geolocation of Surface Measurement: Solving for the Surface Specular Reflection Point

The estimated location of the center of the surface glistening zone of the reflected signal provides the main point of reference for the geo-location of the GNSS-R measurement. This point on the surface is referred to as the specular point (SP) and can be estimated mathematically using the physical geometry of the transmitting and receiving satellites and a modeled of the Earth's ocean surface. An initial solution for the SP is calculated using the WGS84 ellipsoid model. This solution is then adjusted to more refined models, which depend on whether the SP is on the ocean or from a terrestrial surface.

3.1 Earth Models

In order to precisely predict the SP, it is necessary to account for deviations in the Earth's mean sea surface height as compared to the WGS84 model [5]. When over ocean we use the

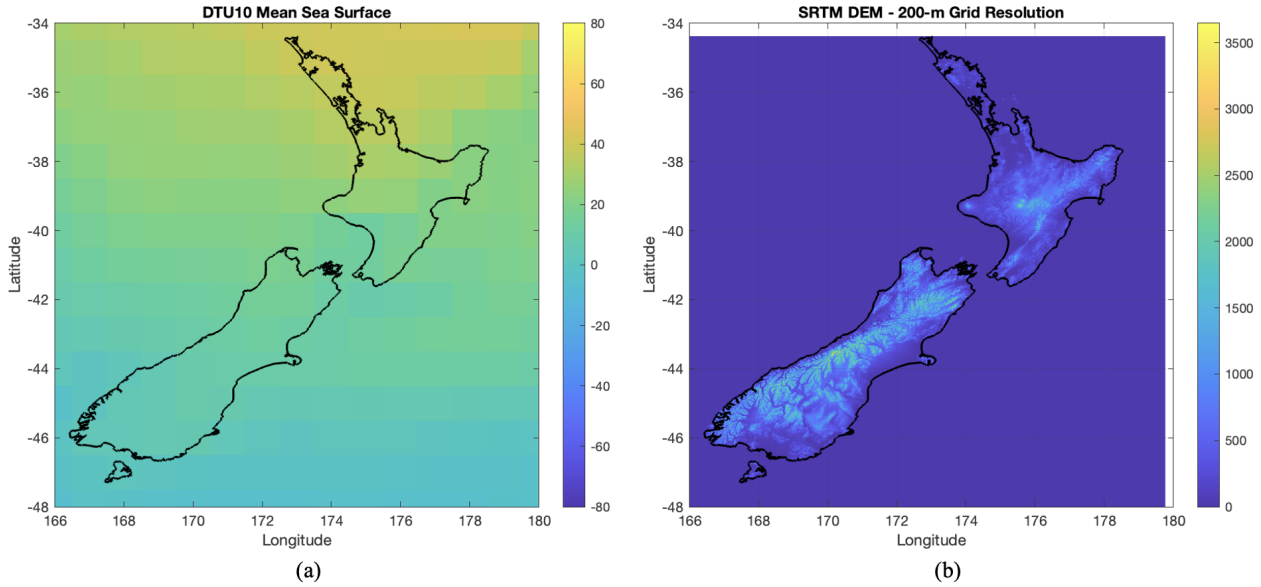

Figure 2: (a) DTU-10 Mean Sea Surface Height, and (b) 200-m SRTM DEM modified from the original 30-m version.

DTU10 mean sea surface model. For land surfaces, we use the Shuttle Radar Topography Mission (SRTM) digital elevation map (DEM) [6].

3.1.1 DTU10 Mean Sea Surface

The mean sea surface is the displacement of the sea surface relative to a mathematical model of the Earth and it closely follows the Earth's geoid. The amplitude of the deviation from the WGS84 ellipsoid is generally within approximately ±100 meters over the Earth's ocean surfaces.

The original DTU10 data was reduced to a 1 degree by 1 degree resolution to improve the efficiency of the calculation, and which is reasonable, due to the fact that height variations are relatively small. The DTU10 map of sea surface height variations relative to the WGS84 ellipsoid use in the specular point solver is shown in Figure 1(a).

3.1.2 SRTM Digital Elevation Map

The DEM product generated by Shuttle Radar Topography Mission (SRTM) is used when the specular reflections are over land. As shown in Figure 1(b), to improve the computational efficiency,the original 30-m DEM has been regridded to 200-m resolution for the L1 geolocation.

3.1.3 Distance to the Coast and the Ocean-land Mask

The information of the distance to the closest coast is derived from high resolution Global Self-consistent Hierarchical, High-resolution Shoreline (GSHHS) dataset [7]. The region is illustrated in Figure 2(a),

- A positive value represents a land SP, whereas
- A negative value represents an ocean SP.

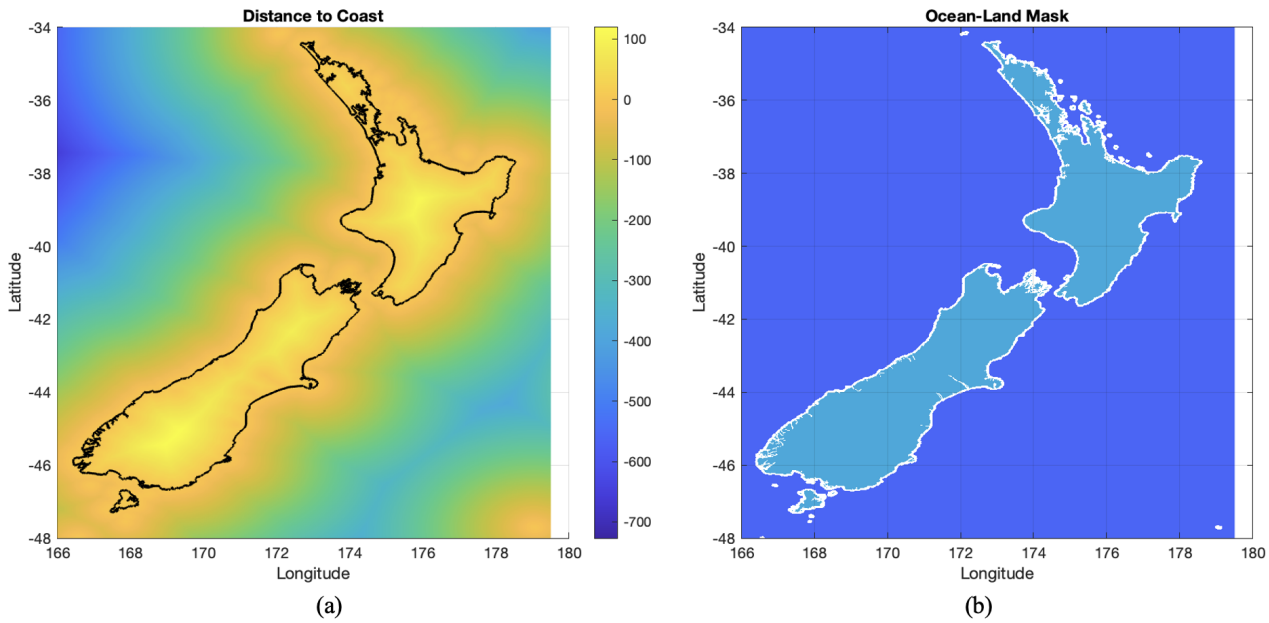

Figure 3: (a) Distance to coast, measured in km, and (b) Ocean-land mask.

Based on this distance-to-coast information, an ocean-land mask has been generated. This mask is used in both land and ocean ground segments based on the following rules:

- Ocean surface: Over ocean for distances from the coast-line greater than 5 km.
- Land surface: Over terrestrial surfaces for inland distances from the coasts further than 0.5 km.
- Common surface: between 5 km off-shore and 0.5 km onshore.

This file was modified and converted in a regular grid 1/8 degree of resolution, it is displayed in Figure 2 (b).

3.2 Specular Point Solver Implementation

As illustrated in Figure 4(a), there are two steps to derive specular points (SPs) over the Earth surface [8]:

- Deriving SPs on the smooth WGS84 ellipsoid model.
- Fine tuning the WGS84 SPs on the local surface depending on the surface type (ocean or land).

3.2.1 Deriving SPs on Smooth WGS84 Surface

A simplified geometrical relation to compute the coordinates where the specular point is located on the surface is illustrated in Figure 4(b), where it shows the three parameters required to solve a specular point on WGS84 surface: a) the Earth-centered Earth-fixed (ECEF) position of the aircraft, reported every second by NGRx, b) the estimate of the transmitting satellite using ground based precise ephemeris, and c) the WGS84 ellipsoid model of the Earth.

A Fibonacci sequence has been employed to compute the initial location of SP. The overall flowchart of the WGS84 initial SP derivation is illustrated in Figure 5.

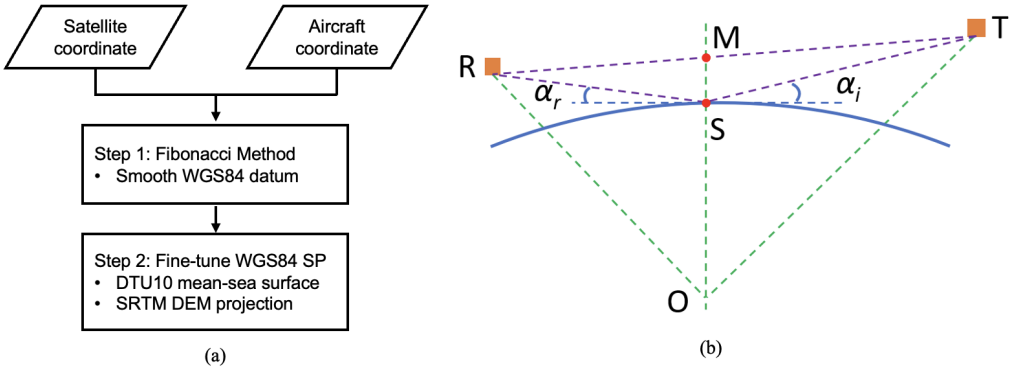

Figure 4: Deriving a SP (a) Flowchart, and (b) geometrical relationship.

Here, the start and end points of the searching domain are defined by:

$$\begin{cases} \lambda_k = a_k + \frac{F_{n-k-1}}{F_{n-k+1}}(b_k - a_k), \\ \mu_k = a_k + \frac{F_{n-k}}{F_{n-k+1}}(b_k - a_k), \end{cases} \tag{4}$$

where $k = 1, 2, ..., n-1$, $a_1 = \vec{R}$ and $b_1 = \vec{T}$ are the coordinates of the receiver and transmitter in the Earth-centered Earth-fixed (ECEF) coordinate frame, respectively. F_k is the Fibonacci sequence, which follows:

$$F_k = \frac{1}{\sqrt{5}} \left\{ \left(\frac{1+\sqrt{5}}{2} \right)^{k+1} - \left(\frac{1-\sqrt{5}}{2} \right)^{k+1} \right\}, \tag{5}$$

At each iteration, the α_i and α_r of the nadir of λ_k or μ_k is compared to determine the parameters that needs to be updated in the $(k+1)$th iteration. Iteration ends when $|\alpha_i - \alpha_r|$ is smaller than a predefined threshold ε.

3.2.2 Fine-tune WGS84 Specular Points over Ocean Surface

The WGS84 Earth model, although generally accurate enough for most applications, relies on approximations that result in residual specular point position estimation errors that are large enough to significantly impact the pixels in the DDM used to calculate the bistatic radar cross section (BRCS). Therefore, subsequent to the WGS84 solution, an improved SP solution is calculated using the more accurate DTU10 mean sea surface model [3], and a brute force, computationally-efficient algorithm:

1) The original specular point solution based on the WGS84 ellipsoid model is the initial estimate of the specular point.

2) A large 3-D grid of points is constructed around the estimated specular point. This grid has uniform latitude and longitude spacing and is conformal to the WGS84 ellipsoid at each point.

3) At each grid point, the surface elevation is modified to the DTU10 mean sea surface height. The 1-degree resolution DTU10 data (shown as Figure 2(a)) is bi-linearly interpolated to find the elevation at each grid point. The resulting grid is then conformal to the DTU10 surface.

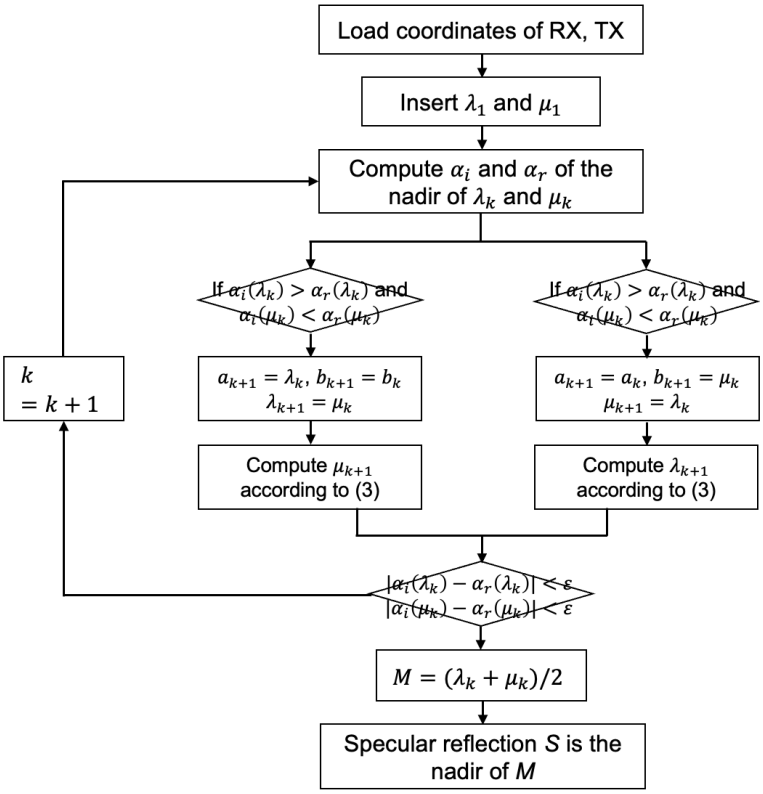

Figure 5: Flowchart of Deriving a WGS84 SP.

4) Next, the point in the grid with the minimum reflection path length (from transmitter to the grid point to the receiver) is found. This minimum-path-delay grid point becomes the new specular point location estimate.

5) An additional higher resolution grid is constructed around this estimated specular point location and steps 2-4 are repeated several times. In this way, a series of search grids sequentially zoom in to refine the specular point. The choice of initial grid size and resolution are carefully chosen to prevent erroneous convergence.

The specular point over ocean surface is defined as the point on the Earth with the minimum reflection path delay. As the surface we use is conformal to an arbitrary geoid topology at each grid point, no mathematical constraint is placed on transmitter and receiver incidence angles in this solution. In a strict sense, it is no longer a "specular" point since (if the ocean surface were smooth) a specular reflection would occur at surface locations with equal transmitter and receiver incidence angles, not minimum delay. Nevertheless, the minimum delay point is sufficient for our purposes as the corresponding specular bin defines the leading edge of the reflected waveform and the specular point represents the center of our iso-delay surface contours within the reflection glistening zone.

3.2.3 Fine-tune WGS84 Specular Points over Terrain Surface

When a SP is located on a terrestrial surface, its position is determined using:

$$\overrightarrow{S} = \overrightarrow{S}_{wgs84} + \frac{\overrightarrow{S}_{wgs84}}{|\overrightarrow{S}_{wgs84}|}\Delta h, \tag{6}$$

where $\overrightarrow{S}$ is the coordinate of the land SP, $\overrightarrow{S}_{wgs84}$ is the vector from the Earth centre to the SP's coordinate on the WGS84 ellipsoid, and Δh is the DEM height above the WGS84 ellipsoid at the WGS84 SP.

It has been demonstrated in [4] that the above projection works well when the terrain has a flat or moderate surface. However, there can be significant variation if the terrain surface is complex. Thus, a confidence flag is implemented to define the confidence of the solved SP location over land.

3.2.4 Confidence Flag for Terrestrial Specular Points

The terrestial geolocation confidence flag uses four criteria: 1) delay criteria: the difference between the NGRx-observed delay and the delay derived for the SP; 2) Doppler criteria: the difference between the NGRx-observed Doppler and the Doppler derived for the SP; 3) Snell angle criteria: the elevation and azimuth Snell angle differences at the SP; and 4) the signal to noise ratio (SNR) at the SP.

a. Delay criteria

The expected code phase delay at any given surface point $\overrightarrow{S}$, can be expressed as

$$\tau_S = \tau_{dir} - \delta P, \tag{7}$$

where τ_S is the code-phase-delay at $\overrightarrow{S}$, τ_{dir} is the code-phase-delay of the tracked direct signal at the same time epoch, and δP is the additional code-phase-delay between the direct and surface reflected code-phase-delays. The additional code-phase-delay is given by:

$$\delta P = |\overrightarrow{T} - \overrightarrow{S}| + |\overrightarrow{R} - \overrightarrow{S}| - |\overrightarrow{T} - \overrightarrow{R}|, \tag{8}$$

where $\overrightarrow{T}$ and $\overrightarrow{R}$ are the positions of the transmitter and the receiver, respectively.

Consequently, the delay difference between NGRx-observed and L1-derived SPs are given by:

$$\delta\tau = \tau_{S,NGRx} - \tau_{S,L1} = \delta P_{NGRx} - \delta P_{L1}, \tag{9}$$

where δP_{NGRx} is provided in the Level 0 metadata. Thus, it is expected that $\delta\tau$ is small enough to determine if the Level 1-estimated SP is the "real" SP location observed by NGRx.

b. Doppler criteria

A similar surface contour map can be generated using the frequency dimension of Rongowai land observations. The expected Doppler frequency at any given local surface point ($\overrightarrow{S}$) can be calculated as:

$$D_S = D_R + D_T + D_{clk}, \tag{10}$$

where D_R is the Doppler component due to the receiver velocity, D_T is the Doppler due to the transmitter velocity and D_{clk} is the Doppler bias from the drift of the satellite instrument clock.

The individual Doppler terms induced by the receiver and transmitter are calculated as:

$$D_R = -1(\overrightarrow{R}_v \cdot \hat{D}_{RS})\frac{f}{c}, \tag{11}$$

$$D_T = -1(\overrightarrow{T}_v \cdot \hat{D}_{TS})\frac{f}{c}, \tag{12}$$

where $\overrightarrow{R}_v$ is the receiver velocity, $\overrightarrow{T}_v$ is the transmitter velocity, f is the GNSS signal transmit frequency, and c is the speed of light (299,792,458 m/s). Also $\hat{D}_{RS}$ and $\hat{D}_{TS}$ are unit vectors directed between the receiver and surface point and transmitter and surface point, respectively:

$$\hat{D}_{RS} = \frac{\overrightarrow{R} - \overrightarrow{S}}{|\overrightarrow{R} - \overrightarrow{S}|}, \tag{13}$$

$$\hat{D}_{TS} = \frac{\overrightarrow{T} - \overrightarrow{S}}{|\overrightarrow{T} - \overrightarrow{S}|}. \tag{14}$$

Similarly, the Doppler difference between NGRx-observed and Level 1 SPs are given by:

$$\delta D = D_{S,NGRx} - D_{S,L1}. \tag{15}$$

c. Snell angle criteria

The final check on the terrestrial surface geolocation is purely geometrical and is not linked to the signal peak in the received GNSS-R DDM. This check is often the most robust as it is sometimes the case that the NGRx-observed delay and Doppler values can be difficult to estimate with certainty due to low receiver antenna gain and/or low reflectivity. Figure 6 illustrates the reference frame used to calculate the incidence and scattering angles from a local surface. In this reference frame the following are defined: S is the center pixel in a 3 by 3 group on the local surface grid, and S_1, S_2, S_3 and S_4 are pixels directly to the north, south, east and west, respectively, spaced typically at the DEM resolution (200 m). T and R are the GNSS transmitter and instrument receiver locations respectively, while P_1 and P_2 are the line-of-sight paths from the transmitter to a given surface point and from the surface point to the receiver, respectively. θ_i, ϕ_i, θ_r, ϕ_r are the incidence and scattering polar and azimuthal angles, respectively, which are calculated for every local surface point ($\overrightarrow{S}$).

As shown in Figure 6, all 9 points are referenced to the WGS84 ellipsoid horizontally but "floating" vertically (shown in green). From the 5 local reference points, incidence and scattering angles can be calculated based on the incoming line-of-sight rays to the center pixel from the transmitter and receiver. We define local east, north, up (ENU) unit vectors from the center reference pixel, S, as follows:

$$\hat{E}_r = \frac{\overrightarrow{S}_3 - \overrightarrow{S}_4}{|\overrightarrow{S}_3 - \overrightarrow{S}_4|}. \tag{16}$$

$$\hat{N}_r = \frac{\overrightarrow{S}_1 - \overrightarrow{S}_2}{|\overrightarrow{S}_1 - \overrightarrow{S}_2|}. \tag{17}$$

$$\hat{U}_r = \hat{E}_r \times \hat{N}_r. \tag{18}$$

Subsequently, the projected line-of-sight ray paths from the transmitter to the center surface pixel from the center pixel to the receiver (P1 and P2, respectively, in Figure 6) are projected to the local surface ENU surface reference frame directions:

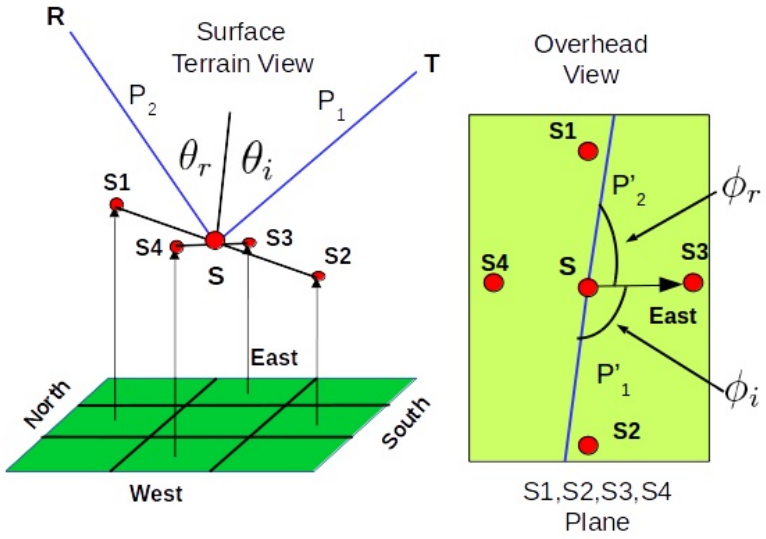

Figure 6: (left) Surface terrain view of point on local surface grid showing incident and reflection angles with respect to the surface normal. (right) Overhead view with incident and reflected vectors projected to a local two dimensional surface with forward scattering azimuth angles shown.

$$P'_{1,E} = (\overrightarrow{S} - \overrightarrow{T}) \cdot \hat{E}_r \tag{19a}$$

$$P'_{1,N} = (\overrightarrow{S} - \overrightarrow{T}) \cdot \hat{N}_r \tag{19b}$$

$$P'_{1,U} = (\overrightarrow{S} - \overrightarrow{T}) \cdot \hat{U}_r \tag{19c}$$

$$P'_{2,E} = (\overrightarrow{R} - \overrightarrow{S}) \cdot \hat{E}_r \tag{20a}$$

$$P'_{2,N} = (\overrightarrow{R} - \overrightarrow{S}) \cdot \hat{N}_r \tag{20b}$$

$$P'_{2,U} = (\overrightarrow{R} - \overrightarrow{S}) \cdot \hat{U}_r \tag{20c}$$

From these unit vectors it is possible to calculate the polar and azimuth angles shown in Figure 6 as:

$$\theta_i = \text{atan}(P'_{1,U}, \sqrt{(P'_{1,E})^2 + (P'_{1,N})^2}). \tag{21}$$

$$\theta_r = \text{atan}(P'_{2,U}, \sqrt{(P'_{2,E})^2 + (P'_{2,N})^2}). \tag{22}$$

$$\phi_i = \text{atan}(P'_{1,N}, P'_{1,E}). \tag{23}$$

$$\phi_r = \text{atan}(P'_{2,N}, P'_{2,E}). \tag{24}$$

We are interested in the difference between the calculated angles and an ideal forward specular reflection from the given surface point. The resulting angle differences from a specular reflecting geometry are then:

$$\delta\theta = \theta_i - \theta_r \tag{25}$$

$$\delta\phi = \text{atan}(\sin(\phi_r - (\phi_i + \pi)), \cos(\phi_r - (\phi_i + \pi))), \tag{26}$$

We define the total angular error metric as the sum of the absolute errors in the azimuth and elevation angles relative to that of an ideal specular reflection,

$$\delta\Phi = |\delta\theta| + |\delta\phi|. \tag{27}$$

d. Geolocation Estimation Criteria

The three geolocation parameter checks described above are computed over the local surface grid around the initial estimate of the specular reflection point. If each criteria check is within limits for a given grid point, it is likely that this is the location of the GNSS-R observation. The limits are determined by the geolocation requirements for a given application. Table 1 summarises the three criteria and the limits used during the analysis that follows.

Table 1: Summary of land geolocation criteria parameters and thresholds used during performance analysis.

Criteria	Threshold	Verification
$\|\delta\tau\|$	1.25 C/A chips	Maximum delay
$\|\delta D\|$	200 Hz	Maximum Doppler
$\delta\Phi$	2 degrees	Reflection geometry

The limits in Table 1 were selected to achieve an approximate geolocation accuracy of 1 km or less (although results will vary depending on the amplitude of the terrain variations). The algorithm also assigns a confidence level to each geolocation, as specified in Table 2 based on whether any points can be identified within the local surface grid that satisfy the three conditions and based on the DDM SP's signal to noise ratio (SNR).

3.2.5 Theoretical SP Location in the DDM

When the SNR is low, the specular point location on the surface cannot be reliably estimated using the peak power bin. Instead we calculate the theoretical SP bin. The DDM pixels at and surrounding the theoretical SP determine the region used to make the surface bistatic radar cross section measurement, the DDM Average (DDMA).

Estimation of the DDMA from the Level 1a DDM uses a more precise location of the specular point described here. This region of the DDM represents the bins of highest reflected power and smallest spatial footprint on the surface. Accurate knowledge of this region is critical for NBRCS calibration and wind speed retrievals over the ocean. Figure 7 shows a typical Rongowai delay waveform at the center Doppler bin for the ocean surface. The vertical line on the delay axis is the estimated specular point delay bin using the L1-derived specular point location detailed in prior sections.

Table 2: Summary of terrestrial geolocation confidence flag logic.

SNR Threshold (2dB)	Delay, Doppler, Snell	Confidence	Comment
Above	Invalid	0	Most likely incorrect
Below	Invalid	1	Likely incorrect
Below	Valid	2	Likely correct
Above	Valid	3	Most likely correct

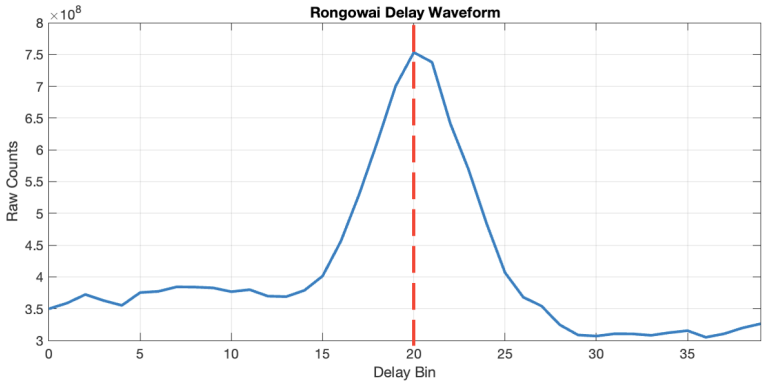

Figure 7: Specular point location in an example ocean Rongowai delay waveform.

The precision (fractional) delay bin offset of the specular point in the DDM is calculated by:

$$\alpha_{SP}^{delay} = 20 - \frac{\delta P_{NGRx}}{\Delta} - \frac{\delta P_{SPOC}}{\Delta}, \tag{28}$$

where 20 is the DDM centre delay bin (0-base bin numbering), Δ is the DDM bin resolution, δP_{NGRx} and δP_{SPOC} are the additional range to SP (measured in chips) estimated by the NGRx and the L1 processor, respectively (see Eq. (8)).

4 L1b Calibration Algorithm: from Watts to NBRCS

The Level 1a calibrated DDM represents the received surface signal power in Watts binned over a range of time delays and Doppler frequencies. Before any geophysical parameters can be estimated these power values must be corrected for non-surface related terms by inverting the forward model shown in Eq. 2.

The Rongowai Level 1b calibration generates three data products associated with each Level 1a DDM:

1) A bin by bin calculation of the surface bistatic scattering cross section, σ (not normalized by scattering area);

2) bin by bin values of the effective scattering areas; and

3) NBRCS for the DDM Area (DDMA) (40 delay $\times$ 11 Doppler bin region) around the estimated specular point location in the DDM.

The first two products will allow users to calculate NBRCS for specified surface extents using the scattering areas of the individual DDM bins. The values of σ are corrected for

the effects of the transmit and receive antennas, range losses and other non-surface related parameters. The effective scattering areas are calculated based on the measurement specific reflection geometry and include the GPS specific delay and Doppler spreading functions. However, care should be taken when using DDM bins away from the specular point, as some of the corrections applied (such as the receive antenna gain and path losses) will degrade at pixels outside the DDMA area.

4.1 Calculation of Bistatic Radar Cross Section

Referring to Eq. (2) has been modified as below to suit the requirement of deriving both co-pol and cross-pol BRCS (σ) for Rongowai. As the DDM L1b BRCS product will not be normalised, we have removed $\overline{A}$ from Eq. 2 and replaced the normalized radar cross section σ_0 with a the non-normalized σ. Additionally, receive antenna gain, the GPS antenna gain, and total pathloss are approximated with their values at the specular point and applied across the whole DDM.

$$\begin{bmatrix} \sigma^{co-pol}_{\hat{\tau},\hat{f}} \\ \sigma^{x-pol}_{\hat{\tau},\hat{f}} \end{bmatrix} = \frac{(4\pi)^3 (R^T_{SP} R^R_{SP})^2}{\lambda^2 P^T G^T_{SP}} \begin{bmatrix} G^{L,co-pol}_{R,SP} & G^{R,x-pol}_{R,SP} \\ G^{L,x-pol}_{R,SP} & G^{R,co-pol}_{R,SP} \end{bmatrix}^{-1} \begin{bmatrix} P^{g,L}_{\hat{\tau},\hat{f}} \\ P^{g,R}_{\hat{\tau},\hat{f}} \end{bmatrix}, \tag{29}$$

where

1) $P^{g,L}_{\hat{\tau},\hat{f}}$ and $P^{g,R}_{\hat{\tau},\hat{f}}$ are the L1a calibrated signal power at a specific delay ($\hat{\tau}$) and Doppler ($\hat{f}$) bin for LHCP and RHCP channels, respectively,

2) R^T_{SP} and R^R_{SP} are the range loss from the transmitter to the surface and the surface to the receiver at the specular point, respectively.

3) P_T and G^T_{SP} are the GPS satellite transmit power and antenna gain at the specular point, respectively. These values are estimated using a ground based GPS Power Monitor and measurements from the CYGNSS navigation antenna to map the transmit power of individual GPS satellites.

4) $G^{co-pol}_{R,SP}$ and $G^{x-pol}_{R,SP}$ are co-pol and cross-pol receiver antenna gain at the specular point, respectively. Both gains are applied across all DDM bins. The antenna gain outside the DDMA region will introduce errors that should be accounted for when using pixels outside the DDMA region (3 delay and 3 Doppler around SP).

4.2 Antenna Pattern

In L1a ATBD section 2.2.2, the antenna cross-pol ratio plot indicates a rotation of the chamber measured antenna pattern. Here we apply a rotation to the antenna cross-pol pattern and calculate the root mean square difference (RMSD) between model and measurement, and a minimum RMSD is achieved after rotating the antenna pattern by 51° counter clockwise, as shown in figure 8. Note that there are two minimum points because the antenna cross-pol ratio is rotationally symmetric, thus they are equivalent to each other. In the following reflectivity retrieval method, the antenna patterns are rotated by 51°.

4.3 Physical and Effective Scattering Area

A single delay Doppler bin will contain the captured scattered power across one or more physical regions on the ocean surface. For each delay Doppler bin in the DDM this region will

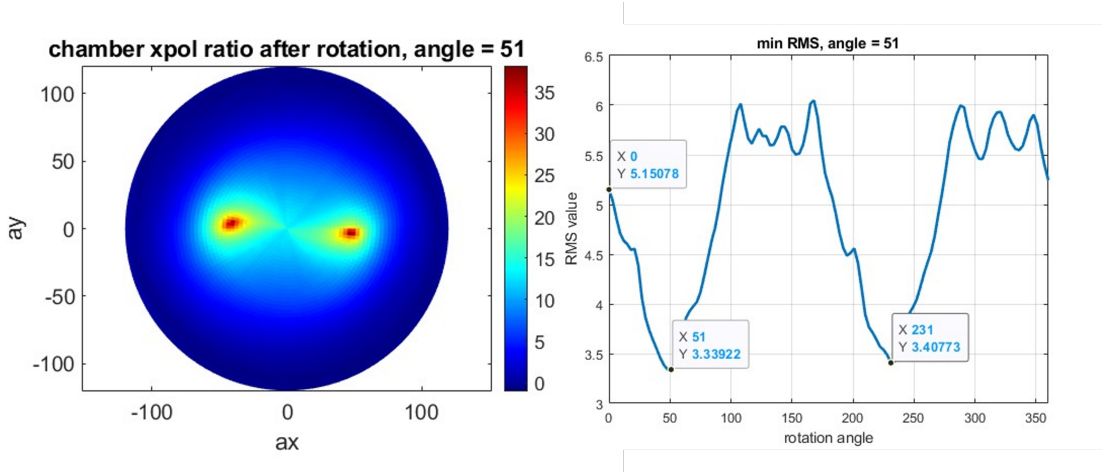

Figure 8: Left: Antenna cross-pol ratio pattern after rotation; Right: RMS value vs rotation angle

vary both in actual physical size (on the ground surface area) and effective area (combined with the GPS spreading functions). The GPS ambiguity functions (in both delay and Doppler) increase the effective area of each delay Doppler bin, causing power to be "spread" into adjacent delay and Doppler bins from outside the geometry determined physical scattering area. These functions change the levels of overall processed power observed. The physical area of each DDM bin can be calculated as follows,

$$A_{\hat{\tau},\hat{f}} = \iint_A \mathrm{d}x\mathrm{d}y. \tag{30}$$

An example of the physical scattering are for a typical DDM is shown in Figure 8(a). Note that points up to and before the specular point bin (i.e. at delays shorter than the specular reflection point delay) have no physical surface scattering area. The power received in the bins before the specular point is due to power being spread into these bins by the GPS ambiguity functions from physical areas near the specular point. The effective surface scattering area for each delay/Doppler bin is expressed as the ambiguity function weighted surface integration,

$$\overline{A}_{\hat{\tau},\hat{f}} = \iint_A \Lambda^2_{\hat{\tau};x,y} S^2_{\hat{f};x,y} \mathrm{d}x\mathrm{d}y. \tag{31}$$

where the delay spreading function $\Lambda_{\hat{\tau};x,y}$ and the Doppler spreading function, $S_{\hat{f};x,y}$ are integrated over the physical surface corresponding to each individual delay/Doppler bin. Figure 8(b) shows the effective scattering area DDM corresponding to the physical scattering areas illustrated in Figure 8(a).

Initial analysis has shown that when only using a relatively small area of the DDM, it is sufficient to approximate the receive antenna gain, range loss terms and the GPS transmit antenna power and gain using constant values calculated at the specular reflection point.

4.4 Expression for NBRCS

The L1b bin by bin DDM of and the bin by bin DDM of effective scattering areas can be combined to calculate a normalized radar cross section value, σ_0, over selected regions of the

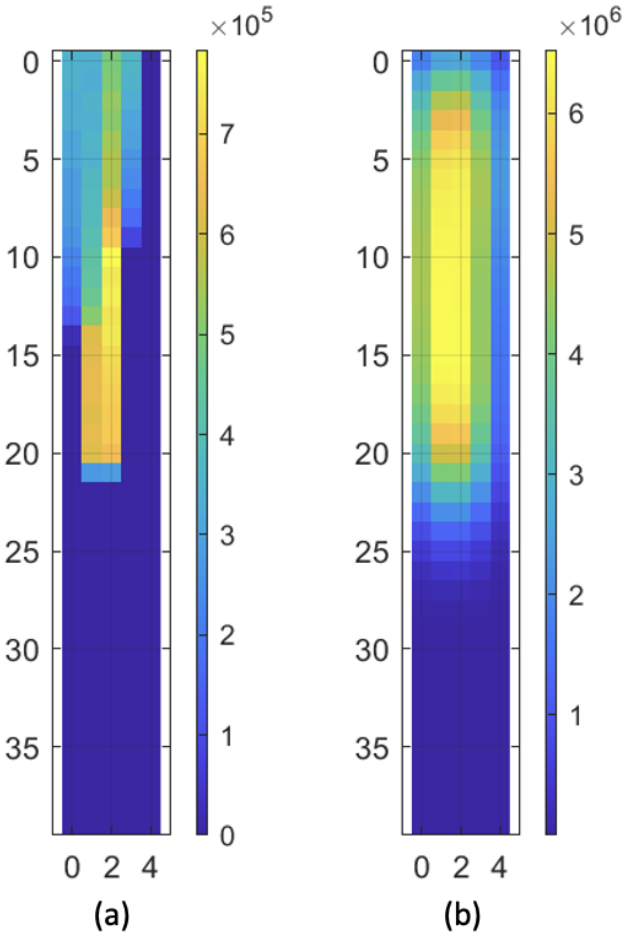

Figure 9: (a) Physical scattering area for a typical DDM reflection geometry. (b) Corresponding Effective scattering area

measurement DDM called the DDMA.

The DDMA consists of 3 delay bins and 3 Doppler bins, with the specular point located in the first row (shortest delay) of this region. At this initial stage, Rongowai L1 product only reports the NBRCS at the predicted SP bin derived from Eq. (28).

Figure 9(a) shows this DDMA region within the red dashed square, overlapped with the normal instrument processed DDM. The true (best estimate) of the specular point is marked as a red dot in Figure 9(b), while the white dot is the Level 1b DDM that the "true" specular point falls in.

These precise DDMA bins will not normally align exactly with the L1b DDM bins generated by the instrument (due to errors in the instruments open loop signal tracker), thus using the value of the single SP bin in the L1b DDM will lead to errors. The "true" DDMA radar cross section is the weighted combination of L1b DDM bins around the best estimate surface specular point and fractional contributions from bins around the edge of the DDMA region. This set of overlapping DDM bins is, when weighted, the best estimate of the "true" multi-bin DDMA total radar scattering cross section σ_0. The mis-alignment between the measured L1b DDM bins and the "true" DDMA bins is illustrated in Figure 9(b). The DDMA specular point is offset by fractional bin amounts in delay (δ) and Doppler (Δ) from the L1b measurement DDM shown in the figure.

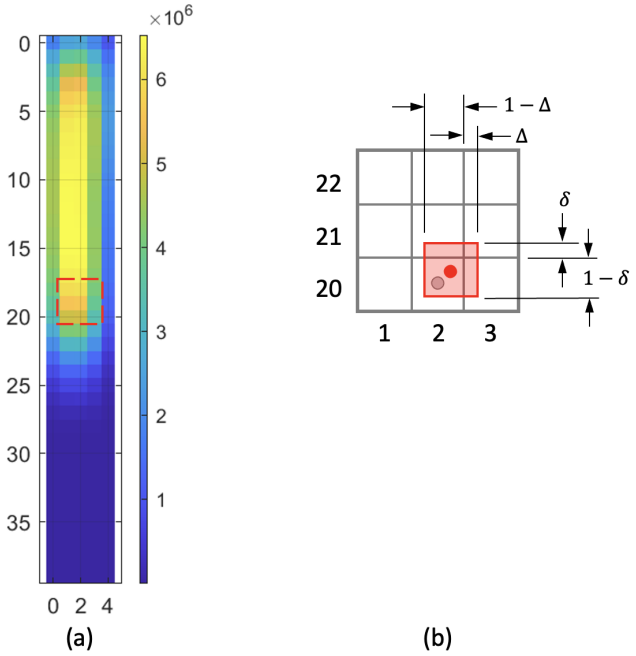

Figure 10: (a) DDMA region. (b) Detail of the overlap areas of a single DDMA bin (the specular point bin) and adjacent L1b bins.

In order to calculate the total radar cross section of the "true" SP bin, the actual measurement L1b values need to be combined using a weighting scheme that includes only a fractional amount of power from bins around the edges of the DDMA bins. The fractional weighting scheme used is approximated to be linear in both the delay and Doppler dimensions.

The total DDMA radar cross section can be calculated as per Eq. 32, resulting in a combined expression for the peak SP bin [2],

$$\sigma^0 = \frac{\sigma_{weighted}}{A_{total}} \tag{32}$$

where

$$\sigma_{weighted} = (1-\delta)(1-\Delta)\sigma_{m,n} + \delta(1-\Delta)\sigma_{m+1,n} + (1-\delta)\Delta\sigma_{m,n+1} + \delta\Delta\sigma_{m+1,n+1}, \tag{33}$$

where m and n are the integer part of the delay row and Doppler column of the SP bin, respectively. $\sigma_{weighted}$ is then normalized by the effective scattering area of SP bin to arrive at the final σ_0.

5 L1b Calibration Algorithm: Reflectivity

5.1 Power Calibration

Following the discussion in L1a ATBD section 2.2.2 Dual-channel Power, there is a bias between model and measured specular power distribution. Here, we attempt to calibrate the power bias empirically. It should be noted that we use peak power of the DDMs obtained from Lake surface instead of the power of the DDM specular bin when calibrating the power. Additional filtering conditions are applied to the Rongowai measurement data. Data satisfying

the following conditions is excluded:

- flight altitude (L1 variable `ac_alt`) $< 0.9 \times$ flight peak altitude
- LHCP DDM SNR (L1 variable `ddm_snr`) < 2 dB
- Angle between two velocity vectors of two adjacent samples > 0.001 rad
- distance between specular point and lake coast line < 300 m
- NGRx Off boresight angle (L1 variable `sp_theta_body`) $> 60°$

The last condition is added because we have more confidence in the signal directions of lower incidence angle, where the antenna cross-pol gain pattern is less likely to be modified by the aircraft metal body and multipath effect.

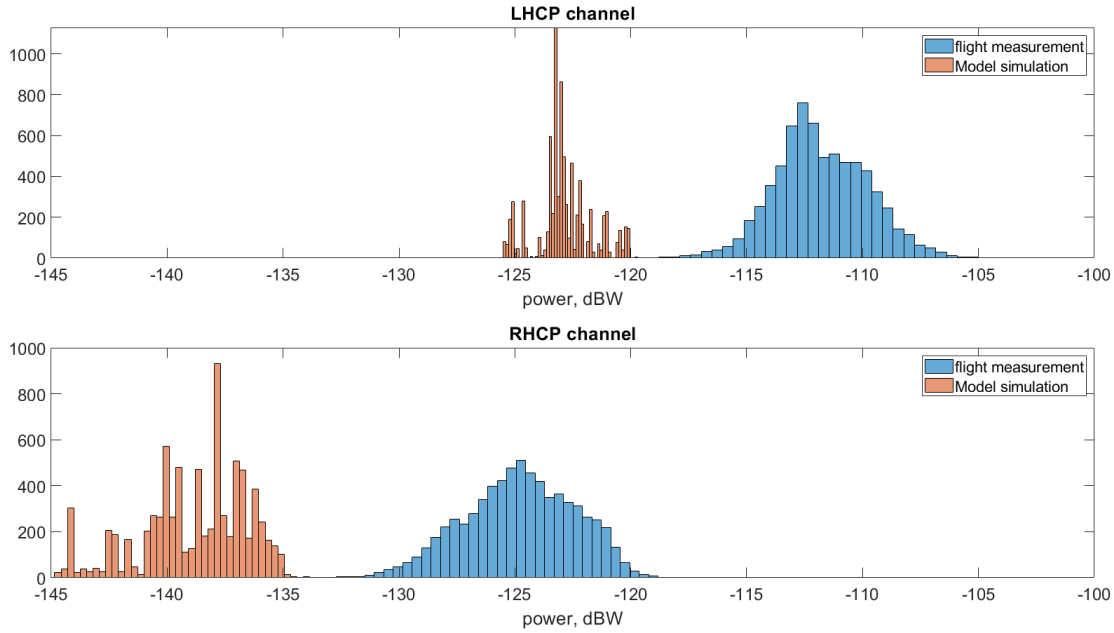

Figure 11: NGRx measrued power (blue) vs modeled power (orange). Upper: LHCP Co-pol channel; Lower: RHCP cross-pol channel

The modeled [9] and measured specular coherent power reflected from Lake Taupo after applying new filtering conditions are plotted in figure 11. A bias is clearly observed between model and measurement. Here we attempt to correct the measured power empirically by shifting the measured power by a scale factor, and then comparing with model by calculating their root mean square difference (RMSD). However, there are three uncertainties in our power model: windspeed, GPS cross-pol EIRP, antenna pattern change. In the power model simulation, windspeed is assumed to be 3 m/s based on the average measured windspeed on south lake coast, but the actual windspeed for each sample is unknown. GPS cross-pol EIRP is assumed to vary from 0 to 1% (-20 dB of Co-pol EIRP). We also have low confidence on the cross-pol leakage level in low cross-pol isolation region of the antenna. These uncertainties result in inconsistent RMSD curves obtained from different parts on the antenna polar coordinate, different time, and different GPS Cross-pol EIRP. Hence, we examine the

RMSD curves with the following four conditions for 1, 2, 4 and 8 ms coherent integration time data obtained from 11/1/2022 to 12/9/2023.

1. off boresight angle $< 60°$, and 0 Cross-pol GPS EIRP
2. off boresight angle $< 60°$, and antenna LHCP cross-pol isolation > 12 dB, and 0 Cross-pol GPS EIRP
3. off boresight angle $< 60°$, and antenna LHCP cross-pol isolation > 12 dB, and 1% Cross-pol GPS EIRP (cross-pol power is 20 dB lower than co-pol power)
4. off boresight angle $< 60°$, and antenna LHCP cross-pol isolation < 10 dB, and 0 Cross-pol GPS EIRP

The example RMSD curves for 1 ms and 2 ms data of the four conditions are plotted in figure 12.

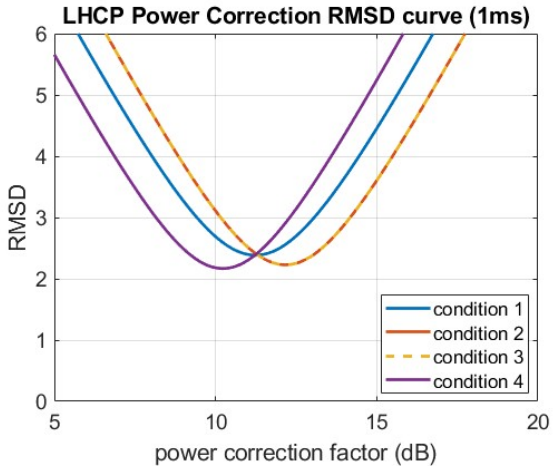

(a) 1 ms, LHCP channel

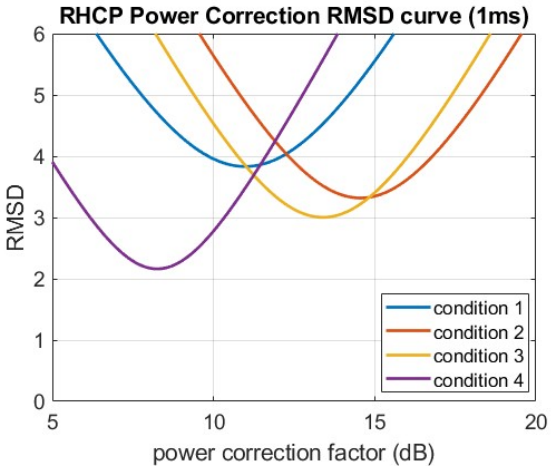

(b) 1 ms, RHCP channel

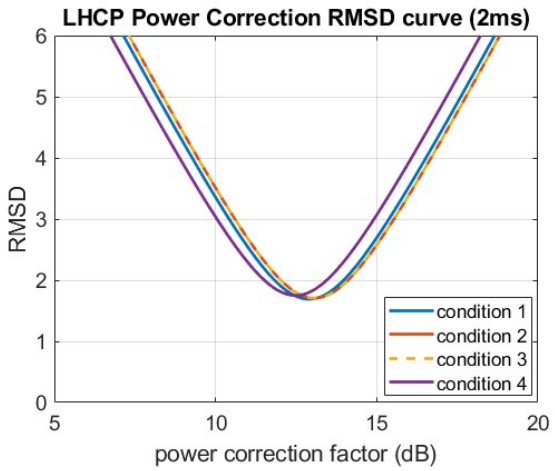

(c) 2 ms, LHCP channel

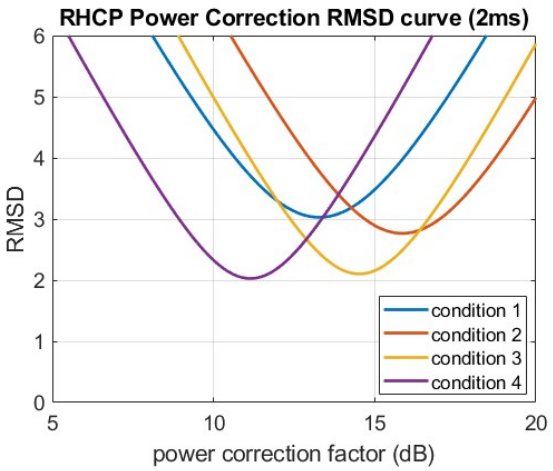

(d) 2 ms, RHCP channel

Figure 12: 1 and 2 ms coherent integration time LHCP and RHCP power correction RMSD curve

The calibration is considered to be robust if the RMSD curves are insensitive to changes of the uncertain parameters in the model. We observe that the RMSD curves for LHCP channel

are similar, while the curves for RHCP channel are clearly inconsistent with each other. This is because: 1) the SNR of the cross-pol channel is much lower than that of the co-pol channel, which means that the cross-pol channel is more sensitive to noise; and 2) the cross-pol channel power is significantly affected by the power leakage from the co-pol channel due to the antenna cross-pol gain which might be corrupted. In addition, comparing condition 2 and 3, 1% GPS xpol EIRP is seen to have little impact on the co-pol channel's RMSD curve, but it changes cross-pol channel's RMSD curve significantly.

The strategy to calibrate the LHCP and RHCP channels is: 1) Assume the biases in both co- and cross-pol channels are the same; 2) Calibrate the co-pol power channel with different condition; and 3) Find an optimal power correction for the co-pol channel and apply same calibration to the cross-pol channel. Based on the results shown in Figure 12, the calibration for the co-pol channel is robust under different conditions. The power correction factors (PCF) that achieve minimum RMSD for the four conditions are tabulated in table 3. We also note that PCFs are different for each coherent integration time, which might result from systematic difference. The fact that the RMSD curves under condition 4 are biased more than those for other conditions might result from the uncertainties in the low antenna cross-pol isolation portion of the pattern (most parts only have an isolation of 5 dB), so the results for condition 4 were discarded.

Table 3: power correction factor (PCF) of min RMSD, # of samples included in parentheses

PCF (dB)	1 ms	2 ms	4 ms	8 ms
condition 1	11.0 (38701)	13.4 (34277)	15.5 (1266)	16.2 (4254)
condition 2	12.0 (14260)	14.1 (15220)	12.6 (445)	16.7 (2204)
condition 3	12.0 (14260)	14.1 (15220)	12.5 (445)	16.7 (2204)
condition 4	9.6 (16007)	11.6 (13863)	12.5 (443)	13.9 (1772)

Given the higher cross-polarization isolation observed in certain sections of the antenna, these areas are deemed more reliable than others, so PCFs obtained under condition 2 are used to fit a curve to express their mathematical relationship and to predict PCFs for all coherent integration time:

$$\mathrm{PCF_{dB}} = 2.3227 \cdot \log(\mathrm{t_{coh}}) + 12.3100$$

The curve fitting has a R^2 of 0.95 and an RMSE of 0.57, and is plotted in figure 13. PCFs of 1, 2, 8 ms coherent integration time data are determined by RMSD curves directly, but data with 4 and 16 ms coherent integration time are determined by the above function due to lack of enough calibration data.

5.2 Flat-surface Dual-pol Reflectivity Retrieval

The link equation, Eq. (3), is inversed as below to derive the flat-surface co-pol and cross-pol reflectivity for Rongowai.

$$\begin{bmatrix} \Gamma^{co-pol}_{\hat{\tau},\hat{f}} \\ \Gamma^{x-pol}_{\hat{\tau},\hat{f}} \end{bmatrix} = \frac{(4\pi)^2 (R^T_{SP} + R^R_{SP})^2}{\lambda^2} \begin{bmatrix} E^{GNSS}_R & E^{GNSS}_L \\ E^{GNSS}_L & E^{GNSS}_R \end{bmatrix}^{-1} \begin{bmatrix} G_{LL} & G_{LR} \\ G_{RL} & G_{RR} \end{bmatrix}^{-1} \begin{bmatrix} P^{g,L}_{\hat{\tau},\hat{f}} \\ P^{g,R}_{\hat{\tau},\hat{f}} \end{bmatrix} \tag{34}$$

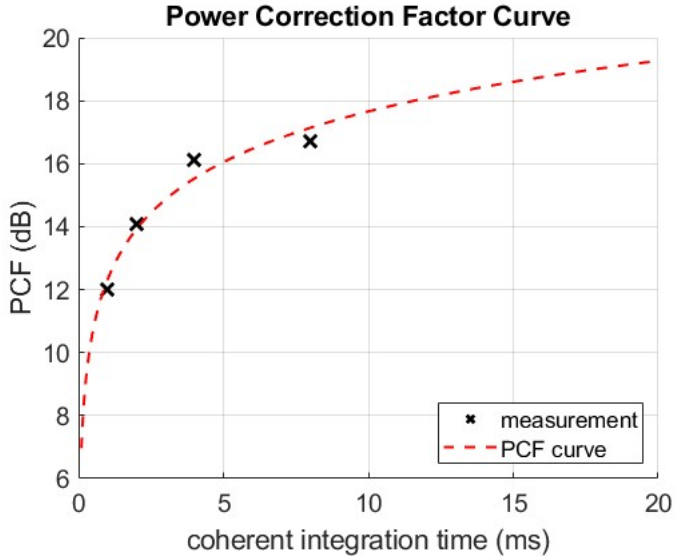

Figure 13: Fitted calibration curve of PCF (dB) vs coherent integration time (ms)

where $\Gamma^{co-pol}_{\hat{\tau},\hat{f}}$ and $\Gamma^{x-pol}_{\hat{\tau},\hat{f}}$ are the co-pol and cross-pol reflectivity at a specific delay ($\hat{\tau}$) and Doppler ($\hat{f}$) bin, respectively. E^{GNSS} represents GNSS EIRP, and G represents antenna gain. Their subscripts L and R stand for the LHCP and RHCP polarization states. The co-pol GPS EIRP (E^{GNSS}_R) has previously been measured for the CYGNSS mission. Currently the cross-pol GPS EIRP (E^{GNSS}_L) is assumed to be zero, but it will be changed later as the measurement of GPS Cross-pol EIRP experiment is still in progress. The antenna gains are using the rotated version described in the above section. Surface reflectivities can be retrieved with all known parameters and input variables in equation (34) for each Rongowai sample.

6 L1b Calibration Algorithm: Coherence Detector

GNSS-R returns have been previously shown to exhibit a variety of behaviors that are impacted by observed surfaces' properties but were found to undergo the most fundamental transitions as a result of varying surface roughness levels. Smooth surfaces, characterized by centimeter scale root-mean-square (RMS) heights, are conducive to mirror-like reflections where received fields arrive with (quasi-)deterministic phases and undergo a process of constructive interference. Measurements corresponding to such observation scenarios are said to dominated by coherent reflections. Conversely, rougher surfaces give rise to a set of scattered fields with random phases that undergo a process of destructive interference at the receiver's end and are said to be dominated by incoherent scatter. In addition to these limiting cases, the classification of other intermediate classifications is also of interest. In spite of Rongowai's spatial footprint being significantly finer compared to spaceborne GNSS-R observatories, the heterogeneities of land returns within an effective range cell together with the along track distance travelled over an interval equivalent to the integration time of a Level-1 DDMs measurement is sufficient to produce 'mixed coherence'. For these more complicated scenarios, with varied relative proportions, smooth surfaces contribute coherent reflection and rough surfaces contribute incoherent scatter.

The distinct surface properties each scattering mechanism is associated with and the dis-

tinct spatial scales to which each mode corresponds to, motivate the incorporation of per-sample indicators of measurements' 'coherence' state. A variety of coherence states were considered and it was determined that as part of Rongowai's initial Level-1 data release, a shape based "matched filter" classification strategy is most suitable given the platform's elevation and the receiver's Level-1 delay-Doppler Map (DDM) maximum delay extent.

Since coherent returns arise due to mirror-like reflection off the earth's surface their shapes are characterized by a sharp peak about the specular and a rapid power decay a small number of chips away from the peak. Their correlation to a known template, the Woodward Ambiguity Function (WAF), will be high relative to incoherent returns. A test of WAF-like behaviours applied to Rongowai's Level-1 data forms the underpinnings of the adopted coherence detection strategy. First, a WAF template, given by (35)-(37) is generated:

$$\chi^2(\tau, f_D) \approx \Lambda^2(\tau) \cdot |S(f_D)|^2 \tag{35}$$

$$|S(f_D)|^2 = \left| \frac{\sin(\pi f_D T_i)}{\pi f_D T_i} \right|^2 \tag{36}$$

$$\Lambda^2(\tau) = \begin{matrix} \left(1 - \frac{|\tau|}{\tau_c}\right)^2 & |\tau| \leq \tau_c \\ 0 & |\tau| > \tau_c \end{matrix} \tag{37}$$

where χ is the WAF, T_i is coherent integration time and τ_c representing C/A code chips duration of 0.97 μs (or equivalently 1 chip) at the respective delay bin resolution and Doppler bin resolutions. The fact that Rongowai is an airborne mission (having lower ground speed) together with its receivers' delay/Doppler extents motivate integrating both the measured delay-Doppler Maps DDM(τ, f_D) and $\chi^2(\tau, f_D) \approx \Lambda^2(\tau)$ along the Doppler dimension f_D, with a maximum extent of N_f bins, as given by (38) such that further processing steps are applied to measured power versus delay $Y(\tau)$ and the Doppler integrated WAF is now effectively equivalent to $\Lambda^2(\tau)$.

$$Y(\tau) = \sum_{j=1}^{N_f} DDM(\tau, j) \tag{38}$$

To facilitate an unbiased shape estimator, compensating for any noise floor fluctuations and varied signal-to-noise levels, a further normalization of the measured $Y(\tau)$ is conducted using (39).

$$\overline{Y}(\tau) = \frac{Y(\tau) - Y_N}{\arg\max_{\tau^*} \left(Y(\tau) - Y_N\right)} \tag{39}$$

where Y_N is an estimate of the power vs delay waveform's mean noise floor computed over a five bin"negative delay space" where reflected signal power fails to map given by (40).

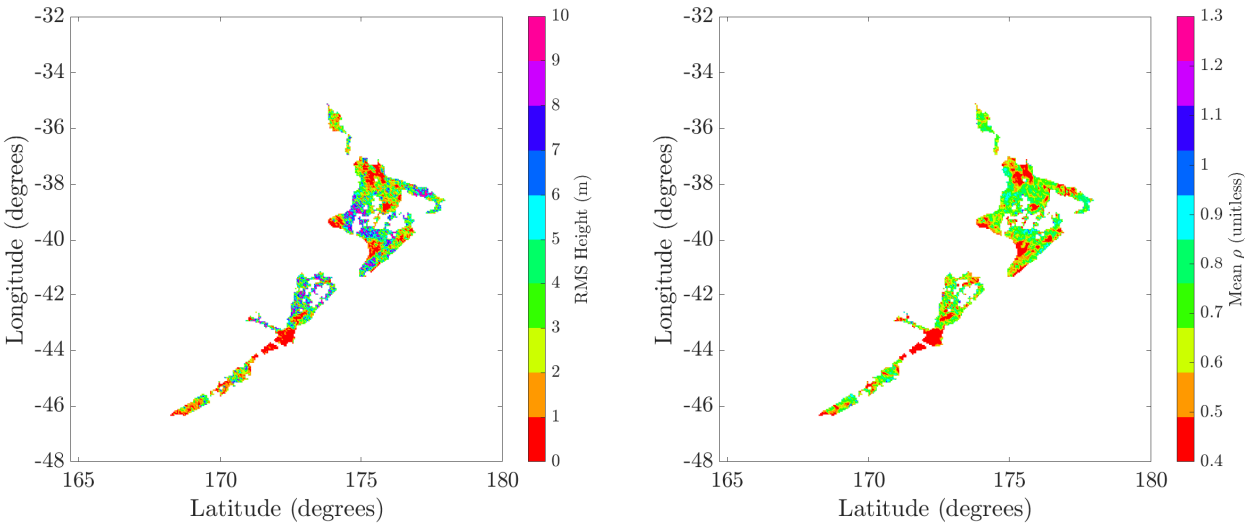

(a) (b)

Figure 14: Maps used in the development and validation of Rongowai's Level-1 coherence detection approach (a) ALOS derived RMS height maps (b) Mean Level-1 coherence metric ρ

$$Y_N = \frac{1}{5}\sum_{i=36}^{40} Y(i) \tag{40}$$

The coherence measure ρ is subsequently derived using a point-by-point comparison relative to $\Lambda^2(\tau)$ over a ± 1 chip delay space, relative to the peak coinciding with bin index τ_M, using (41).

$$\rho = \sqrt{\frac{1}{2\Delta\tau + 1}\sum_{i=-\frac{1}{\Delta\tau}}^{\frac{1}{\Delta\tau}} \left(\overline{Y}(\tau_M + i) - \Lambda(\tau_M + i)\right)^2} \tag{41}$$

where $\Delta\tau$ refers to the measurements' delay resolution. The coherence measure ρ is therefore effectively a measure of shape root-mean-square-difference relative to the WAF, large ρ estimates are indicative of observation scenarios where incoherent scatter dominates while lower ρ indicates a WAF like power distributions and therefore is indicative of an observation scenario where coherence dominates. The sensitivity of Rongowai's measurements to varied levels of surface roughness together with the effectiveness of the adopted approach is evidenced by the spatial correspondence of mean Rongowai ρ and RMS heights h derived using ALOS shown in Figure 14.

While the coarse, relative to the Rongowai 'coherent' footprint, 30 meter ALOS DEM resolution used in the estimation of Figure 14(a) together with the product's vertical uncertainty limits preclude deriving precise RMS height cutoffs that give rise to coherent returns, which could be used in the derivation of ρ detection thresholds, the comparisons showing Figure 14

Table 4: Summary of L1a and L1b calibration terms used to derive primary observable from CYGNSS's un-calibrated raw count DDMs

ρ (unitless)	SNR (dB)	Altitude (km)	Coherence State
$\leq$0.25	$\geq$ -10	$\geq$ 2	With high confidence, state is dominantly coherent
0.25$<\rho\leq$0.5	$\geq$ -10	$\geq$ 2	State is likely to be coherent
0.50$<\rho<$0.75	$\geq$ -10	$\geq$ 2	State is likely mixed/weakly diffuse
$\rho\geq$0.75	$\geq$ -10	$\geq$ 2	With high confidence, state is dominantly incoherent
N/A	$<$ -10	N/A	Uncertain coherence state
N/A	N/A	$<$ 2	Uncertain coherence state

make clear the ability to use some of New Zealand's flatter regions (including subsets of Canterbury, Otago, Taranaki and Waikato) and water bodies (including Lake Taupo crossings when lower surface winds prevail) for the derivation of detection thresholds appropriate for identifying dominant coherence. Higher wind ($>$ 10 m/s), estimated using bi-linearly interpolated ERA-5 ocean wind reference data, were used for identifying detection thresholds applicable for observations dominated by incoherent scatter. Thresholds relevant for intermediate-mixed cases were determined using more complicated case studies. While ρ is provided as part of the campaign's Level-1 data release, enabling end-users to invoke various thresholds they deem appropriate, a total of 5 'coherence states' described in Table 4 using recommended thresholds are also reported with Figure 15 providing representative examples of each.

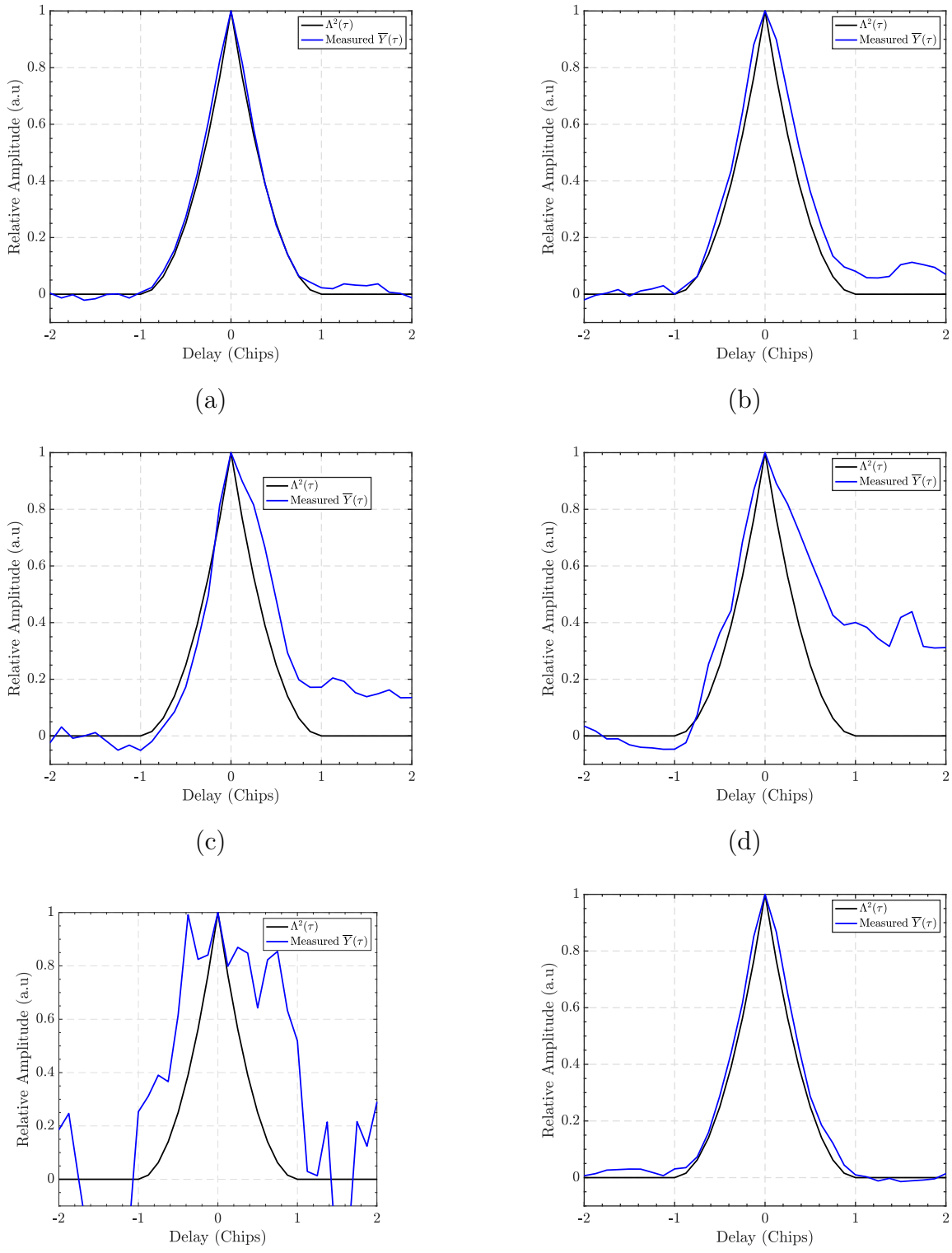

Figure 15: Example measured power versus delay waveforms for different coherence states (a) With high confidence, state is dominantly coherent (b) State is likely to be coherent (c) State is likely mixed/weakly diffuse (d)With high confidence, state is dominantly incoherent (e) Uncertain coherence state, SNR< -10 dB (f) Uncertain coherence state, aircraft elevation $<$2km

References

[1] M. R. Gleason, Al-Khaldi, "Cygnss algorithm theoretical basis document level 1b ddm calibration, rev. 4," 2021.

[2] O. M. Gleason, Ruf, "The cygnss level 1 calibration algorithm and error analysis based on on-orbit measurements," *IEEE Journal of Selected Topics in Applied Earth Observations and Remote Sensing*, vol. 12(1), pp. 37–49, 2018.

[3] D. Moller, C. Ruf, R. Linnabary, A. O'Brien, and S. Musko, "Operational airborne gnss-r aboard air new zealand domestic aircraft," in *2021 IEEE International Geoscience and Remote Sensing Symposium IGARSS*, pp. 1284–1287, 2021.

[4] R. A.-K. J. Gleason, O'Brien, "Geolocation, calibration and surface resolution of cygnss gnss-r land observations," *Remote Sensing*, vol. 12(8), p. 1317, 2020.

[5] O. B. Andersen and P. Knudsen, "Dnsc08 mean sea surface and mean dynamic topography models," *Journal of Geophysical Research: Oceans*, vol. 114, no. C11.

[6] Shuttle Radar Topography Mission (SRTM), Available online: https://www.usgs.gov/centers/eros/.

[7] P. Wessel and W. H. F. Smith, "A global, self-consistent, hierarchical, high-resolution shoreline database," *Journal of Geophysical Research: Solid Earth*, vol. 101, no. B4, pp. 8741–8743, 1996.

[8] X. Lin, D. Moller, A. O'Brien, R. Linnabary, and C. Ruf, "Computing specular points over complex land surfaces for airborne GNSS-R applications," in *IGARSS 2022 - 2022 IEEE International Geoscience and Remote Sensing Symposium*, pp. 1860–1863, 2022.

[9] D. Long and F. Ulaby *Microwave Radar and Radiometric Remote Sensing*, 2015.